Nanoscale

Anomalous Metal Vaporization from Pt/Pd/Al_2O_3 under Redox Conditions

Journal:	*Nanoscale*
Manuscript ID	NR-ART-03-2021-001733.R1
Article Type:	Paper
Date Submitted by the Author:	02-May-2021
Complete List of Authors:	Meng, Andrew; University of Pennsylvania, Materials Science and Engineering Low, Ke-Bin; University of Illinois at Chicago, Research Resources Center Foucher, Alexandre ; University of Pennsylvania, Material Science Li, Yuejin; BASF Research Iselin Petrovic, Ivan; BASF Research Iselin Stach, Eric; University of Pennsylvania, Materials Science and Engineering

ARTICLE

Anomalous Metal Vaporization from Pt/Pd/Al_2O_3 under Redox Conditions

Andrew C. Meng,[1] Ke-Bin Low,[2] Alexandre C. Foucher,[1] Yuejin Li,[2] Ivan Petrovic,[2] Eric A. Stach[1,3]

Received 00th January 20xx,
Accepted 00th January 20xx

DOI: 10.1039/x0xx00000x

Al_2O_3-supported Pt/Pd bimetallic catalysts were studied using *in-situ* atmospheric pressure and *ex-situ* transmission electron microscopy. Real-time observation during separate oxidation and reduction processes provides nanometer-scale structural details – both morphology and chemistry – of supported Pt/Pd particles at intermediate states not observable through typical *ex-situ* experiments. Significant metal vaporization was observed at temperatures above 600°C, both in pure oxygen and in air. This behavior implies that material transport through the vapor during typical catalyst aging processes for oxidation can play a more significant role in catalyst structural evolution than previously thought. Concomitantly, Pd diffusion away from metallic nanoparticles on the surface of Al_2O_3 can also contribute to the disappearance of metal particles. Electron micrographs from *in-situ* oxidation experiments were mined for data, including particle number, size, and aspect ratio using machine learning image segmentation. Under oxidizing conditions, we observe not only a decrease in the number of metal particles but also a decrease in the surface area to volume ratio. Some of the metal that diffuses away from particles on the oxide support can be regenerated and reappears back on the catalyst support surface under reducing conditions. These observations provide insight on how rapid cycling between oxidative and reductive catalytic operating conditions affects catalyst structure.

Introduction

For automotive emission catalysts, accelerated aging at high temperatures for a prolonged period in a specific gas environment is an established means to simulate the effects of catalytic activity decrease over the entire life of the vehicle.[1] This is because prolonged exposure of catalysts at high temperatures under oxidative conditions is known to reduce the metal surface area due to metal sintering and formation of volatile oxides. Thus, aging tests are essential in determining the durability of the catalyst and diagnosing the mechanisms for catalyst deactivation.[1] In this context, recent advances in instrumentation for *in-situ* gas cell TEM allow real-time observations of catalyst behavior during aging to be captured with nanometer-scale spatial resolution.[2] Supported Pt/Pd bimetallic catalysts are widely utilized in automotive emission controls, such as oxidation of NO,[3] CH_4,[4-6] diesel,[7] and other volatile organic compounds.[8-10]

We chose to study Pt/Pd supported on γ-Al_2O_3 because of the high activity exhibited by Pt and Pd individually for oxidation of hydrocarbons and carbon monoxide.[11, 12] Furthermore, it is known that Pd improves the stability of the Pt catalyst by increasing the barrier to sintering and lowering the PtO_2 vapor pressure through the presence of a PdO phase.[13-15] Supported Pt/Pd catalysts have been studied extensively using electron microscopy,[16-21] x-ray absorption fine structure,[22-25] infrared spectroscopy,[26, 27] and temperature-programmed reduction or desorption measurements.[28, 29] Pt sintering at low pressures has also been studied using environmental transmission electron microscopy (ETEM).[30] There are also numerous *in-situ* x-ray studies of supported Pt/Pd catalysts that describe the transformation of the metal particles under reaction environments.[20, 22, 24, 26, 27] However, there are many remaining questions about the real-time structural, morphological, and compositional changes of the metal particles under realistic redox conditions. Much of what is understood about catalyst structural changes are implied from a combination of *ex-situ* TEM and *in-situ* X-ray studies. Because X-ray experiments lack spatial resolution, it can be difficult to determine the mechanism by which changes occur in catalyst particle size and distribution. In addition, ETEM is unable to reach the high pressures (atmospheric pressure) of typical catalyst operating conditions and thus it can be difficult to correlate these observations with realistic operating environments. Real-world applications of platinum group metal catalysts on oxide supports are wide-ranging and include diesel oxidation catalysts[31] and nitrous oxide adsorbers.[32] Recent work on bimetallic Pt/Pd catalysts have shown Al_2O_3 to be the most active out of a series of industrially relevant catalyst support materials, and provided insights towards optimizing the catalytic activity.[33]

[1] *Department of Materials Science and Engineering, University of Pennsylvania, Philadelphia, PA, 19104*
[2] *BASF Corporation, Iselin, NJ 08830*
[3] *Laboratory for Research on the Structure of Matter, University of Pennsylvania, Philadelphia, PA, 19104*
Electronic Supplementary Information (ESI) available: [details of any supplementary information available should be included here]. See DOI: 10.1039/x0xx00000x

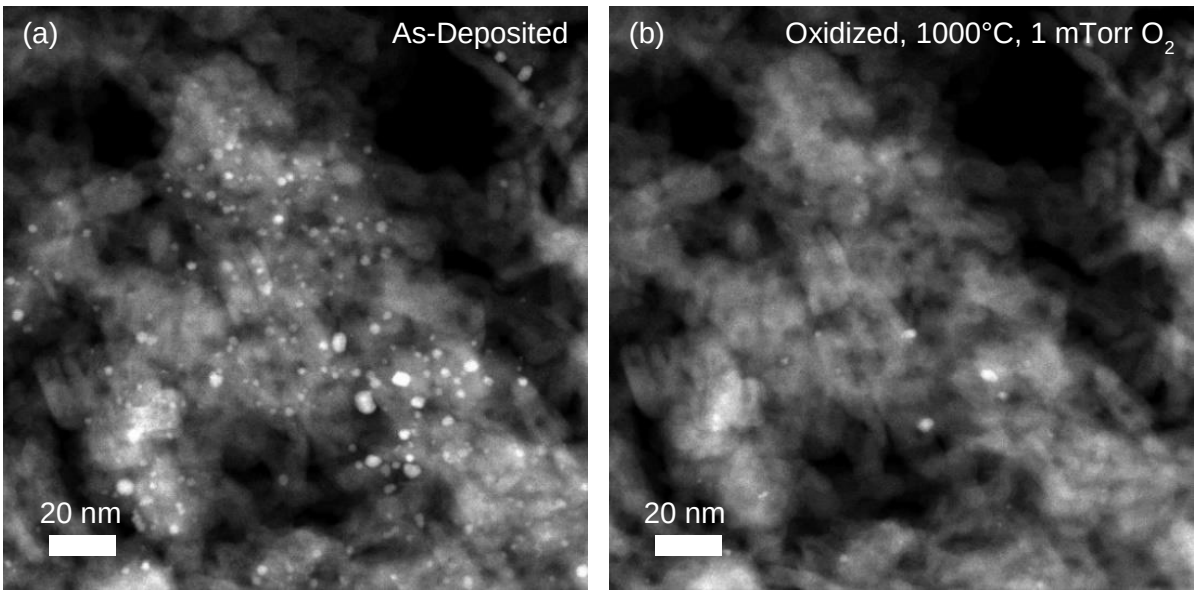

Figure 1 Dark field STEM images of Pt/Pd catalyst a) as-deposited on Al_2O_3 support b) after oxidation at 1000°C under 1 mTorr O_2 in ETEM.

This study was motivated by a preliminary oxidation experiment in which Pt/Pd catalyst supported on Al_2O_3 was observed to disappear during annealing at 1000°C under 1 mTorr O_2 (Figure 1). Although performed in an ETEM (FEI, Hillsboro), no real-time data was collected. The dark field STEM images show that the metal catalyst disappeared from the field of view. Prevailing theories suggest that Pt/Pd vaporization should not be the dominant phenomenon. Here, we use atmospheric pressure TEM to understand the dynamics that occur during redox with high spatial and temporal resolution. Atmospheric pressure TEM has the advantage that the temperatures and pressures that can be utilized are similar to those that the catalyst is exposed to during typical catalyst aging conditions. This contrasts with ETEM, where only relatively low-pressure gas exposures are possible. We use a Machine Learning (ML) based image segmentation to quantify the tremendous amount of image data obtained during these *in-situ* TEM experiments. *Ex-situ* experiments were performed to corroborate the *in-situ* observations.

Experimental

Catalyst Preparation

Model Pt/Pd (1.33 wt%/0.67 wt% loading) catalyst nanoparticles dispersed on porous γ-Al_2O_3 support were calcined for 2h at 550°C in 1 atm air under no flow (these catalysts will be referred to subsequently as fresh catalyst). The resulting oxide support is primarily γ-Al_2O_3 with specific surface area of ~ 100-200 $m^2\ g^{-1}$ (Supporting Information Figure S1 and S2). The catalyst and support were ground using a mortar and pestle, suspended in isopropyl alcohol, and sonicated before being drop-cast onto the TEM heating chips. *Ex-situ* annealing in O_2 was performed for 2h at 700°C (20°C/min. ramp rate) in a Carbolite HZS three-zone tube furnace and in air for 2h and 5h at 700°C in a Thermolyne Type 47900 muffle furnace (Thermo Scientific): for oxidizing conditions, 1 atm O_2 at a 500 sccm flow rate and 1 atm air under no flow was used; for reducing conditions, 1 atm 95:5::N_2:H_2 (v/v) at a 50 sccm flow rate was used.

Structural Characterization

In-situ gas cell experiments in the TEM were performed on a JEOL JEM-F200 200 kV S/TEM in scanning transmission (STEM) mode in a multi-channel gas flow TEM holder (Hummingbird Scientific) using a chip containing a microfabricated heating element and a 50 nm thick spacer with 30 nm thick SiN_x windows. For STEM imaging, probe size 7 was used with a 40 µm condenser aperture, leading to ~ 60 pA probe current. For oxidative conditions, two conditions were used: (1) 1 atm O_2 and 1 sccm flow rate or (2) 1 atm air (20 °C, 40% humidity), with no active flow. During heating, the temperature was increased by 100°C approximately every 5 min for an average ramp rate of 20°C/min, comparable to *ex-situ* experiments. For elemental mapping, *ex-situ* energy-dispersive x-ray spectroscopy (EDS) in STEM was performed on a spherical aberration probe corrected JEOL NEOARM 30-200kV S/TEM equipped with two large-area silicon drift detectors (SDD) for EDS with 1.7 steradian solid angle. For EDS mapping experiments, probe size 6C was used with a 40 µm condenser aperture, leading to ~ 120 pA probe current. Large area *ex-situ* EDS measurements were also performed in TEM mode on a JEOL JEM-F200 200 kV S/TEM using a spot size of 1 and a 100 µm condenser aperture. X-ray diffraction (XRD) θ-2θ scans were collected using a zero-background holder (Rigaku 906165 Flush, Si510) on a Rigaku Miniflex 6G powder diffractometer with a Cu X-ray source operating at 40 kV/15 mA. A Ni foil K-β filter incident beam monochromator and a 1-D solid-state detector are used. EDS mapping in the scanning electron microscope (SEM) was performed using an FEI Quanta 600 FEG Mark II Environmental Scanning Electron Microscope equipped with an EDS detector (EDAX) operated in high vacuum mode at 30 kV accelerating voltage and 2 nA beam current.

Machine Learning Image Segmentation

The Trainable Weka Segmentation Plug-in[34] for ImageJ was used to classify Pt/Pd catalyst particles on Al_2O_3 support during *in-situ* oxidation conditions of 1 atm O_2 and 1 sccm flow rate. The training data was generated from the bright field (BF) STEM images manually by classifying regions as being either part of a catalyst particle or part of the background and included data from multiple images. In order to consistently segment the images, only three classification models were used to segment images: the first model was used for all images taken below 700°C, the second was used to segment images when rapid morphology changes were taking place at 700°C, and the third was used to segment images taken at 700°C when the system was close to being equilibrated. Particle analysis in ImageJ included the following parameters: particle number, area, and aspect ratio (defined as the ratio of the major to the minor axis).

Results

Simulation of Aging Using *In-Situ* Oxidation

In-situ gas cell experiments provide a complete picture of the catalyst aging process. Figure 2 shows a time-lapse of BF-STEM images of Pt/Pd/Al_2O_3 under 1 atm O_2 (1 sccm flow rate) at various temperatures. The presence of a large number of darker contrast regions in the image of the fresh catalyst (Figure 2a) indicates a large number of metallic nanoparticles. The data show that metallic catalyst particles disappear over time, starting at approximately 600-700°C, and that this change occurs within several minutes once this threshold temperature is reached (Figure 2 d-e). To confirm effects of the electron beam, the same oxidation experiment shown in Figure 2 was performed in the TEM with the beam blanked. STEM images prior to and after the oxidation show that for this oxidation, the

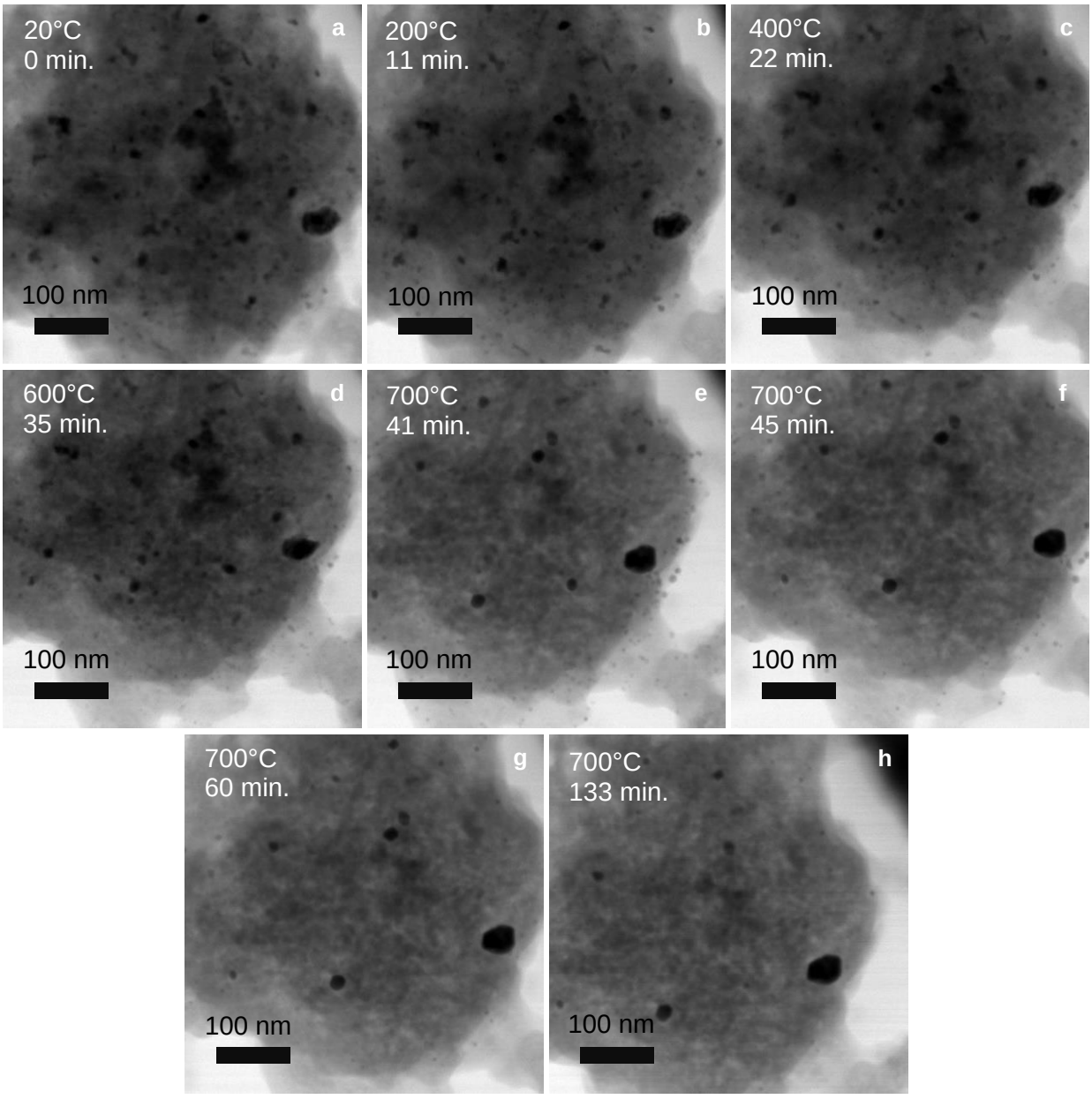

Figure 2 a-h Time-lapse BF-STEM images of Pt/Pd particles on Al_2O_3 support under heating conditions at 1 atm O_2 at 1 sccm flow rate.

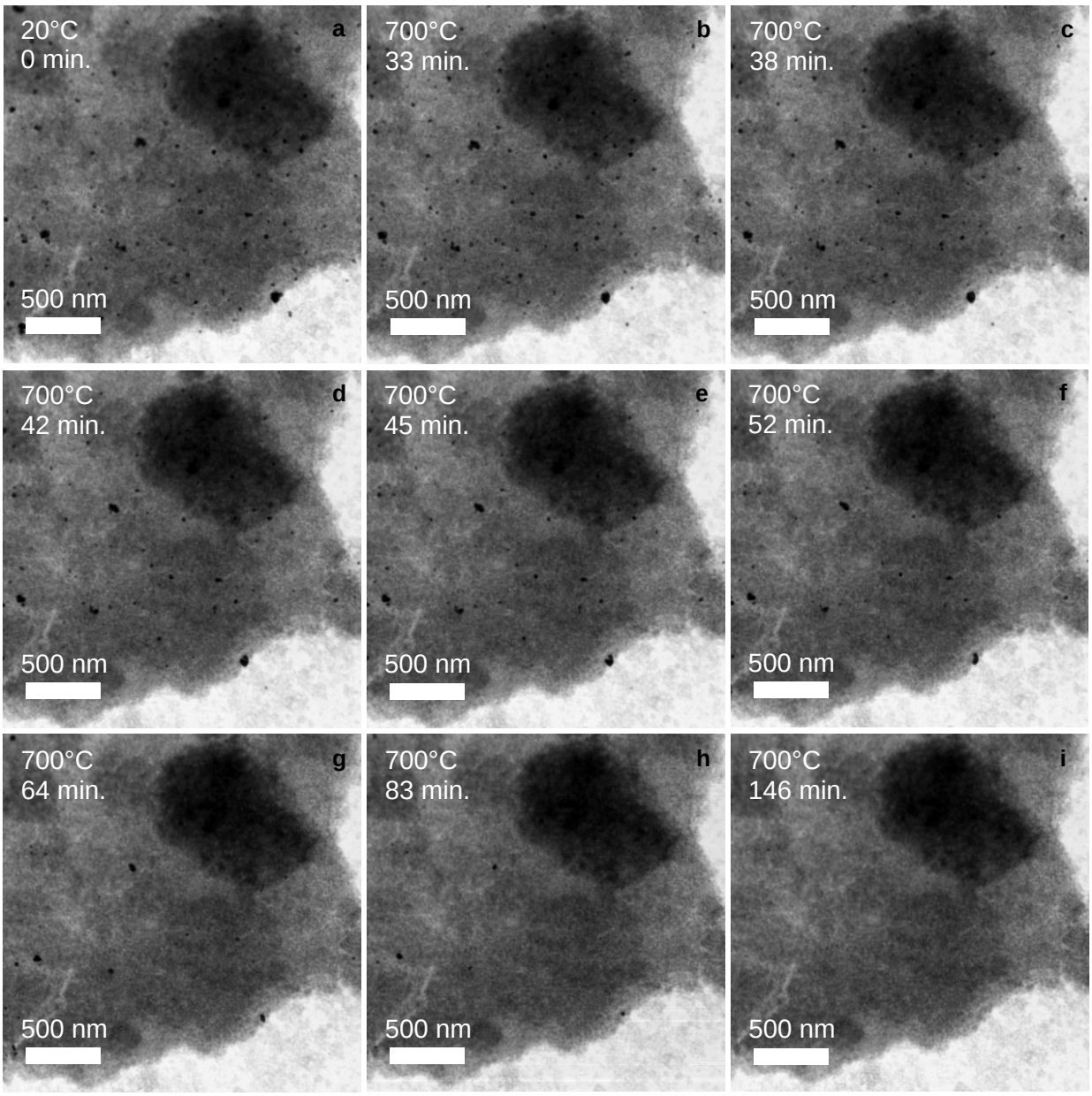

Figure 3 a-i Time-lapse BF-STEM images of Pt/Pd particles on Al_2O_3 support under heating conditions at 1 atm laboratory air and stagnant conditions.

beam does not play a significant role in the structural evolution (Figure S3, Supporting Information). Migration of nanoparticles via center-of-mass motion does not occur to a significant extent: the particles never leave the field of view, and the contrast from a majority of the particles gradually decreases until they become indiscernible from the oxide support. This is most clearly illustrated in the stark difference between Figure 2a and Figure 2h. The data show that, after oxidation, the metal is no longer present in concentrations high enough to be distinguished from the support at the given spatial resolution, which we conservatively estimate to be 1 nm on this thicker support under 1 atm O_2 conditions. [35, 36] Furthermore, there is little evidence for the formation of larger size particles. Although the particles that remain are larger than the average particle size of the fresh sample, and some particles exhibit a modest increase in size during the oxidation process consistent with Ostwald ripening, this apparent increase in particle size reflects mostly the preferential disappearance of smaller particles. Also, the particles remaining on the oxide support after the oxidation appear to be approximately equiaxial in contrast to the originally oblong or irregular shapes of the particles in the fresh sample.

Air Oxidation

To examine the effect of using a lower O_2 partial pressure more typical of catalyst aging conditions, $Pt/Pd/Al_2O_3$ was oxidized *in-situ* in gas-cell TEM at 700 °C using 1 atm laboratory air (20 °C, 40% humidity) under stagnant conditions (no flow). Compared to oxidation in pure O_2, the disappearance of Pt/Pd catalyst particles is delayed and occurs slowly after the temperature reaches 700°C (Figure 3b-i). However, similar disappearance of the metal catalyst was observed as in the experiment under 1

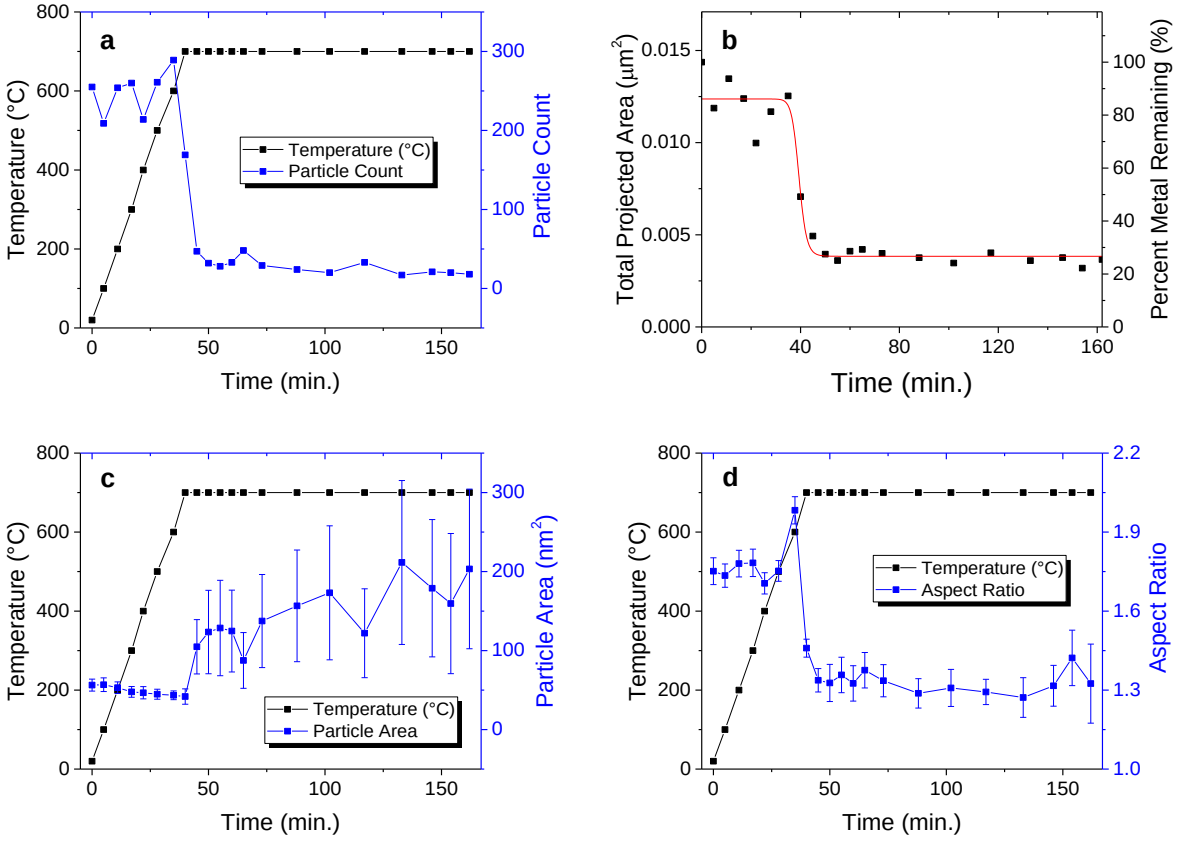

Figure 4 Quantitative descriptors of Pt/Pd catalyst evolution during *in-situ* oxidation/aging in a 2.4×10^5 nm^2 field of view; a) number of catalyst particles; b) percent metal remaining; c) particle area; d) particle aspect ratio.

sccm O_2 (1 atm) conditions (Figure 3a-i). In fact, no particles remain in the field of view after oxidation in air: Figure 3i shows that all Pt/Pd catalyst has disappeared from the field of view. If any metal particles remain, their sizes are below the detection limit (~ 1 nm spatial resolution under 1 atm air).

Machine Learning Image Segmentation and Data Mining

We use the Weka plugin for ImageJ to automate image segmentation for particle analysis. While catalyst particle size distribution is often analyzed, here we also extract the aspect ratio (major and minor axes) allowing a more detailed picture of catalyst evolution that includes shape factor. Figure 4 shows the particle count, metal fraction remaining, area, and aspect ratio throughout an *in-situ* experiment. (Note that the error bars represent the spread (standard deviation) of the sample population and do not represent uncertainty in measurement, which is very small.) The sigmoidal behavior of the amount of metal remaining is consistent with evaporation behavior.[37] In particular, we observe that the aspect ratio decreases towards 1 during oxidation, and that this change occurs somewhat abruptly as the temperature approaches 700°C (Figure 4d). This is consistent with a decrease in the surface area to volume ratio of the particles and is consistent with surface energy as a driving force for the structural evolution of the catalyst.

The image segmentation data provides further insight into the exact nature of the changes in catalyst morphology. Oxidation of the Pt/Pd catalyst decreases the number of particles (from ~600 to ~200 in a field of view of ~2.4×10^5 nm^2) and increases the average particle size (from ~200 nm^2 to ~400 nm^2). However, careful inspection shows that most of the particles do not increase in size. Instead, the *average* particle size has increased because most of the particles have either become too small to be visible or have disappeared (Figure 4b-d).

Comparison with *Ex-Situ* Oxidation

An important consideration is whether the observed vaporization might be entirely caused by the *in-situ* gas cell setup. We verified our observations by repeating oxidation of the catalyst in air at 700°C for 2h and 5h and comparing the metal loading. Afterwards, EDS experiments in TEM mode were performed on multiple regions of the catalyst with areas on the order of ~ 10 μm^2 in order to better statistically sample the composition of fresh and oxidized catalyst. Spectra from fresh catalyst, catalyst that was oxidized in air at 700°C for 2h, and catalyst that was oxidized in air at 700°C for 5h are shown in Figure 5a-c. The plots show intensity in log scale to accentuate the Pt and Pd signals. The Al-K, Pt-M, and Pd-L X-ray signals were used to quantify the composition in these samples using the Cliff-Lorimer method.[38] The Pt/Pd mass ratio decreased from 1.62 in the fresh sample to 1.43 after 2h of oxidation at 700°C to 1.32 after 5h of oxidation at 700°C (Figure 5d). On the other hand, the Pd/Al ratio stayed approximately constant at ~0.04 (Figure 5e).

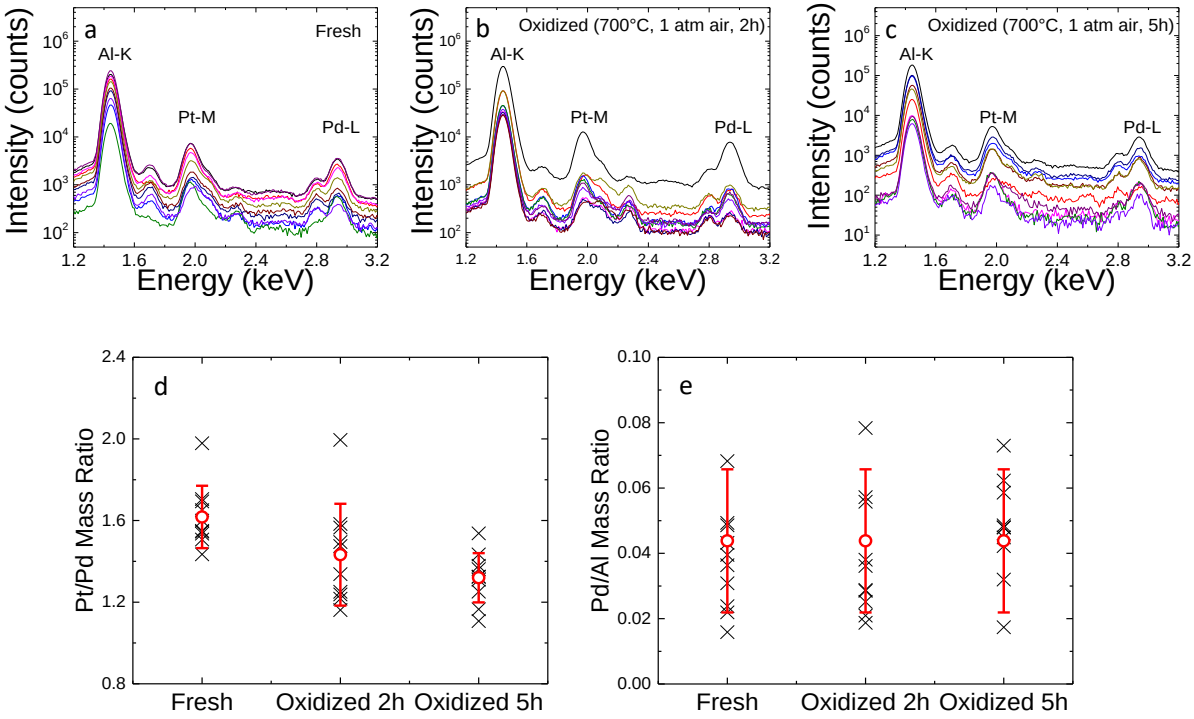

Figure 5 Large area TEM-EDS spectra from multiple regions (indicated by different colors) of a) fresh b) oxidized (1 atm air, 700°C, 2h) c) oxidized (1 atm air, 700°C, 5h) $Pt/Pd/Al_2O_3$; d) Pt/Pd mass ratio and e) Pd/Al mass ratio of a-c.

As an additional confirmation of metal loss during oxidation of $Pt/Pd/Al_2O_3$, XRD was used to compare the fresh and oxidized catalysts. For each sample, 3.4mg was weighed into the center of a zero-background holder with a recess and flattened with a glass slide to ensure an equivalent comparison. The XRD patterns and insets of peaks corresponding to the Pt/Pd are shown in Figure 6. As a result of oxidation in air at 700°C for 2h, the Pt/Pd (200), (220), and (222) peaks decrease in intensity, but the Pt/Pd (111), and (311) peaks increase in intensity. Because some Pt/Pd peak intensities increase while others decrease, it is unclear how the Pt/Pd concentration changes during this step. Additional oxidation for 3h (5h total oxidation time) at 700°C leads to a decrease in the intensity of the Pt/Pd (200) and (220) peaks and no change in intensity of other peaks. Because all Pt/Pd peak intensities either decrease or stay the same during this additional 3h oxidation, this is consistent with a decrease in Pt/Pd concentration in the catalyst during this step.

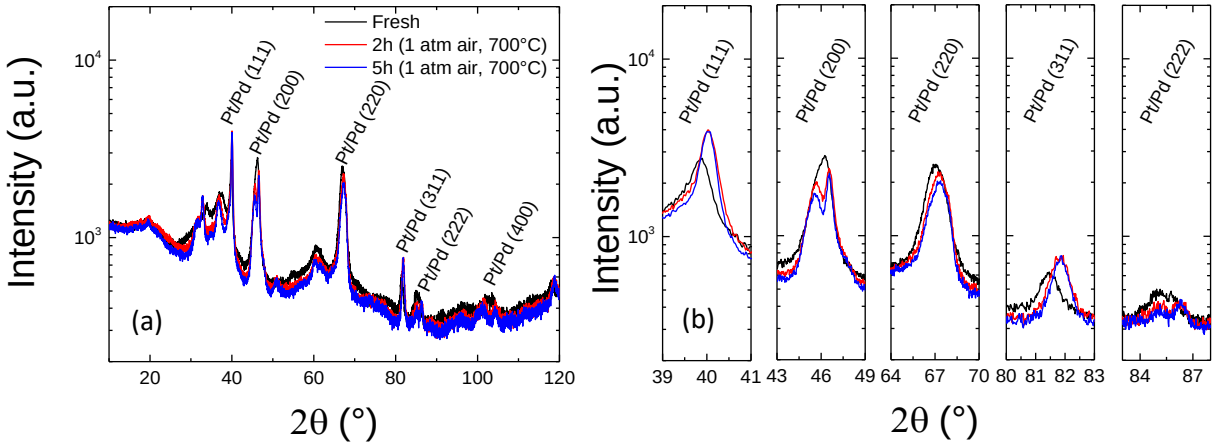

Figure 6 a) XRD θ-2θ scans of fresh, 2h-, and 5h-oxidized $Pt/Pd/Al_2O_3$ and b) insets of Pt/Pd peaks

Characterization of *In-Situ* Gas Cell Chip

To further rationalize the differences between *in-situ* and *ex-situ* oxidation experiments, SEM-EDS mapping of a used gas cell chip was performed. An SEM image with several regions in which individual EDS spectra are collected, and EDS maps are shown in Figure 7. Normalizing the spectra to the intensity of the Pt-M X-ray signal, the Pd-L x-ray intensity varies widely

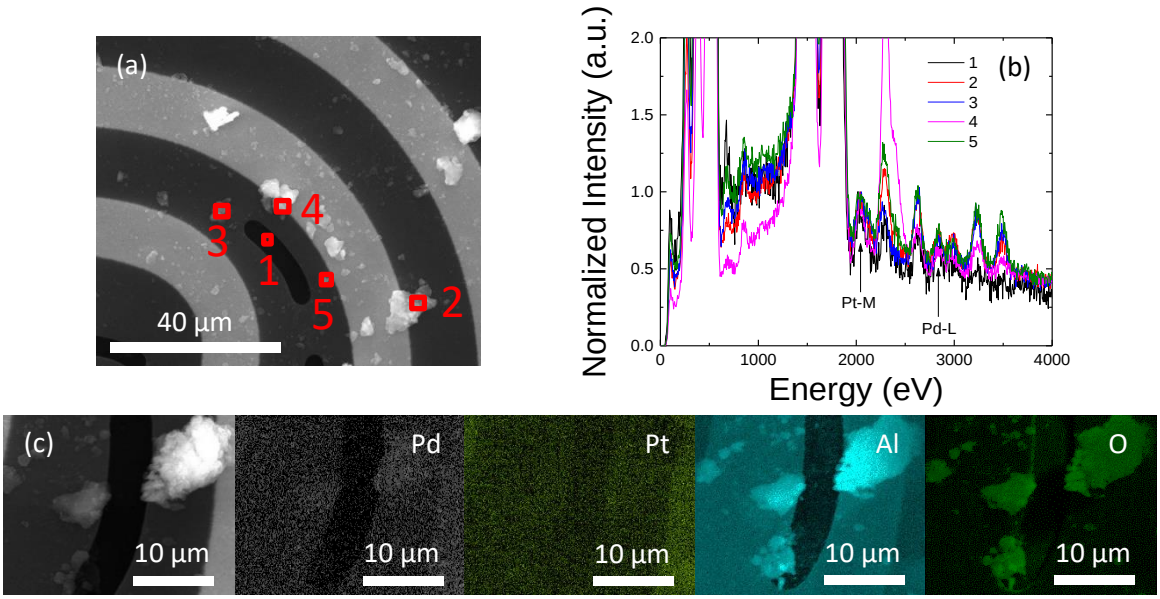

Figure 7 a) SEM image of an oxidized Pt/Pd/Al_2O_3 sample on an *in-situ* gas cell chip; b) individual EDS spectra from the regions marked in a); SEM-EDS composition map of an oxidized Pt/Pd/Al_2O_3 sample on an *in-situ* gas cell chip c) focused on the electron-transparent region

depending on the distance of the sample from the bean-shaped electron-transparent region (Figure 7a-b). In particular, Pd-L X-ray intensity is comparatively greater on oxide support further from the electron-transparent regions. Compositional mapping in SEM-EDS (Figure 7c) shows that metal transport either through diffusion or vaporization and redeposition across the SiN_x membrane occurs to an extent, and that Pt and Pd concentration increases away from the SiN_x membrane towards the heating element. The Pt and Pd elemental maps exhibit diffuse signal consistent with transport away from the electron-transparent region of the sample towards thicker regions.

Elemental Distribution in Fresh and Aged Pt/Pd Catalysts

We performed *ex-situ*, probe-corrected STEM-EDS to determine how the distribution of Pt and Pd in the catalysts changes during the aging process.The fresh Pt/Pd/Al_2O_3 samples exhibited varying compositions and degrees of phase separation (Figure 8a-b). We observe small (< 5 nm diameter) Pt- and Pd-rich species on the support in the fresh sample (Figure S5, Supporting Information). This could be consistent with the segregation of a PdO phase (Figure S6, Supporting Information).[39, 40]

Catalyst Regeneration under Reductive Conditions

Additional STEM-EDS maps consistent with Pt and Pd mixing in the particles are shown in Figure S7 in the Supporting Information. The elemental distribution is non-uniform in both larger particles (~ 20 nm) and smaller particles (~ 1 nm). Post-oxidation, the chemical makeup of the Pt/Pd catalyst is significantly changed. Large Pt-rich and Pd-rich catalyst particles are observed, as are Pt-rich particle cores exhibiting Pd-rich spots on the surface (Figure 8f). The small (< 5 nm diameter) Pt/Pd particles are no longer able to be detected (Figure 8h). Prior to oxidation, regions of the oxide support exhibit both Pt and Pd signal (Figure 8d, Figure S4, Supporting Information), but

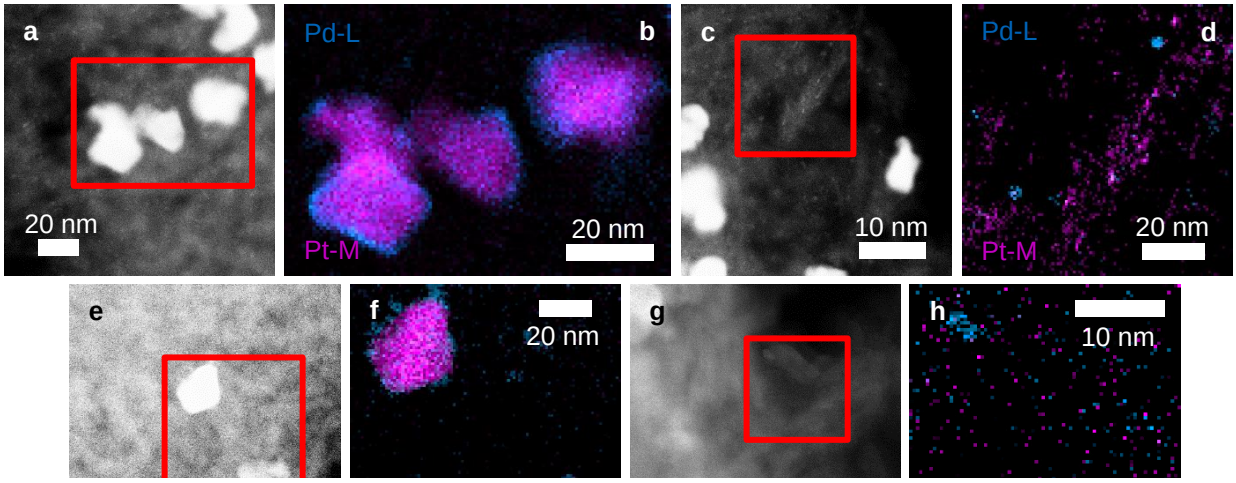

Figure 8 *Ex-situ*, probe-corrected HAADF STEM and STEM-EDS of (a-d) fresh and (e-h) aged Pt/Pd/Al_2O_3. 700°C aging conditions under 1 atm O_2 (500 sccm flow rate) were used.

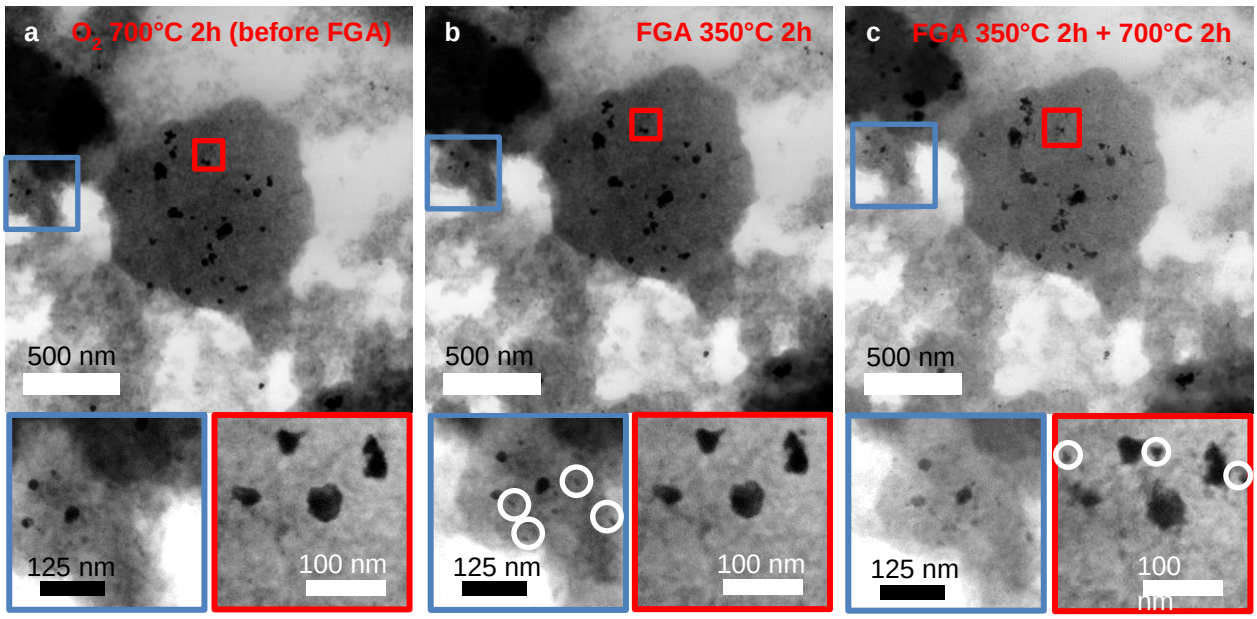

Figure 9 BF-STEM Images of a) Pt/Pd/Al_2O_3 oxidized at 700°C in 1 atm O_2 for 2h and b) same sample after *ex-situ* reduction for 2h at 350°C in 1 atm forming gas (95:5::N_2:H_2, v/v) c) same sample after *ex-situ* reduction for 2h at 350°C and 2h at 700°C in 1 atm forming gas.

after oxidation, only a small signal from Pd remains (Figure 5h, Figure S5, Supporting Information). An aberration corrected STEM image of small metal clusters in oxidized catalyst is also shown in Figure S8 in the Supporting Information.

In addition to catalyst aging, characterization of catalyst regeneration was observed by taking the oxidized/aged Pt/Pd catalyst and performing a forming gas anneal (FGA) *ex-situ*. This process resulted in formation of smaller catalyst particles from larger coarsened particles even after 2h of reduction in forming gas at 350°C (Figure 9b). Following an additional 2h of reduction in forming gas at 700°C, a decrease in the Al_2O_3 support stability was observed (Figure 9c). Some of the Al_2O_3 in the region around the STEM image taken in Figure 9b-c disintegrated from the reduction process, as suggested by a decrease in contrast in those Al_2O_3 support regions compared to regions with no material. The dark contrast region in the top left of the image shows that the combined formation of smaller particles and structural changes in the catalyst support appear to be consistent with nanoparticle catalyst regeneration.

Discussion

Disappearance of the Pt/Pd catalyst particles under oxidizing conditions suggests two hypotheses based on the STEM images: either the metal is vaporizing, or the metal from the nanoparticles is diffusing away and becoming smaller than the spatial resolution of the microscope (~1 nm) under atmospheric pressure conditions. We rule out particle migration as the mechanism for catalyst particle disappearance because it is not observed either on the single frame timescale or on the timescale of the oxidation experiment; this is also consistent with a lack of a large number of small particles in oxidized samples characterized by *ex-situ* STEM-EDS experiments where the overall resolution is substantially higher (< 0.63Å at 200kV accelerating voltage). The STEM-EDS data support both the metal vaporization and diffusion hypotheses. Areas of the support without catalyst particles exhibited Pt and Pd signal prior to oxidation but exhibited only Pd signal at a significantly reduced intensity after oxidation (Figures S4 and S5). These observations are consistent with preferential Pt vaporization and Pt/Pd diffusion on the oxide support. For *in-situ* experiments, another possibility is diffusion of metal species from the oxide support to the significantly larger SiN_x window, then further away from the field of view. Regarding diffusion, Pt and Pd could either diffuse away from original particle positions, either on the surface or into the bulk of the oxide support. As we are observing the sample in transmission, surface diffusion cannot be easily distinguished from bulk diffusion. Also, although surface diffusion coefficients are typically higher than those for bulk diffusion, the latter cannot be entirely ruled out. Thus, the data could be consistent with some extent of Pd dissolution into the oxide support. The hypotheses for Pt vaporization and Pt/Pd diffusion are consistent with the known volatilization of Pt through formation of PtO_2 as well as the role of Pd in stabilizing Pt from forming PtO_2.[3, 13, 14 41]

Vaporization of the metal is also consistent with the significant amounts of metal that disappear during oxidation. This is the case for both oxidation in 1 atm O_2 under active gas flow and in 1 atm stagnant air, which suggests that these changes are unrelated to either the O_2 partial pressure or the replenishment of O_2, both of which are significantly higher for the former condition. Because *in-situ* and *ex-situ* oxidation experiments under active flow are conducted under significantly differing flow rates due to requirements arising from size differences, oxidation under stagnant air in open systems both *in-situ* and *ex-situ* were performed to provide a fair comparison between

the two types of experiments. The results are consistent with some metal loss of Pt/Pd on Al_2O_3 from vaporization. Metal is observed to disappear *in-situ* during oxidation in the TEM and XRD and TEM-EDS in *ex*-situ oxidation experiments are consistent with loss of Pt from the sample.

While higher O_2 partial pressure appears to result in slightly faster onset of Pt/Pd catalyst disapperance, the effect is not overly pronounced. In fact, a larger fraction of metal particles disappears during the air oxidation experiment in which almost all of the Pt/Pd catalyst particles in the field of view disappear. Approximately 2:1::Pt:Pd ratio is used, so even if all of the Pt vaporized, we would still expect about a third of the metal to remain due to the relative stability of Pd to volatilization, assuming the particles were far apart and non-interacting. There could be several reasons for this metal vaporization related to the *in-situ* experiment setup: 1) Pt/Pd is more exposed to O_2 due to low specimen thickness, circumventing mass transport limitations that might normally be present; 2) vaporized Pt/Pd from *in-situ* TEM experiments has no way of being redeposited onto the support like bulk experiments; 3) temperature non-uniformities (e.g. cold spots) and gradients in the hot zone of the *in-situ* TEM holder are likely to be significantly smaller than those in a catalytic converter.

Furthermore, considering the differences between *in-situ* and *ex-situ* oxidation, we find that during *in-situ* oxidation, almost all of the metal disappeared, whereas only a small fraction of metal loss is observed during *ex-situ* oxidation. A decrease in the Pt/Pd ratio while the Pd/Al ratio remains constant is consistent with loss of Pt from the system. Because the precision of the composition measurement by EDS is not very high, we focus on the differences in how the data is distributed. Performing a t-test on Pt/Pd ratio datasets yields p-values of 0.17 for the fresh and 2h oxidized samples, 0.001 for the 2h and 5h oxidized samples, and 0.0001 for the fresh and 5h oxidized samples. This means that while there is a 17% chance of Pt/Pd ratio from the fresh and 2h oxidized catalyst being identically distributed, there is a 0.1% chance of the Pt/Pd ratio from the 2h and 5h oxidized catalyst being identically distributed, and a 0.01% chance of the Pt/Pd ratio from the fresh and 5h oxidized catalyst being identically distributed. The difference in means of the Pt/Pd ratio between the 5h oxidized catalyst and the fresh or 2h oxidized catalyst is statistically significant with $p < 0.01$ (99% confidence interval). Therefore, the *ex-situ* experiments are consistent with some amount of metal loss. On the other hand, no significant difference, even at a $p < 0.05$ (95% confidence interval) level, is observed between the fresh catalyst and the 2h oxidized catalyst, which contrasts with the *in-situ* observations. While the *ex-situ* data is consistent with metal loss, it appears that the rate at which this occurs is dramatically lower than what is observed *in-situ* in the TEM. This could be a result of the geometry of the gas cell, in which gas enters the resistively heated electron-transparent region of the chip, but is unable to recirculate before exiting. This configuration significantly impedes material redeposition, which is a possible explanation of slower evaporation during *ex-situ* oxidation compared to *in-situ* oxidation.

Specifically examining the *in-situ* gas cell configuration provides some insights into the rapid evaporation observed *in-situ*. Because the chip consists of thin, electron-transparent SiN_x regions surrounded by successively thicker regions and an encircling, embedded resistive heating element, the thermal mass and resistance of the sample is the lowest in the electron-transparent region and increases towards the thicker areas closer to the heating element. Thus, impedance to heat flow is likely greater in the thicker, non-electron-transparent regions of the sample. As a result, material transport towards thicker regions of the sample is likely favored. In combination with the small spatial extent of the heated region (~ 10^4 μm^2 × 50 nm) and comparatively rapid gas flow (1 sccm), which results in complete exchange of gas in the heated region of the cell every 30 ns, with no recirculation, this can significantly accelerate transport of metal outside the hot zone.

Nonetheless, our observation of metal loss through vaporization and diffusion differs from the literature, in which vaporization was only observed at temperatures above 750°C.[7, 42] For *in-situ* experiments, this might be attributed to differences in the nature of gas flow over the sample surface; for *ex-situ* experiments, likely the significantly longer oxidation (5h) plays a role. Because the catalyst must be in equilibrium with its vapor in the steady state, and whether the vapor can be swept away determines whether metal loss occurs, we can understand that metal loss at lower temperatures occurs but at an exponentially slower rate according to the dependence of vapor pressure of the metal on temperature.

Although there are differences between *in-situ* TEM conditions and *operando* conditions for a catalytic converter, there are several important implications. Vaporization is likely to be accentuated in the *in-situ* setup due to a relatively uniform hot-zone with a cold exhaust line. On the other hand, this is a good re-creation of the higher temperature regions of a catalytic converter. Thus, catalyst vaporization and redeposition is likely an important part of catalyst structural evolution under oxidizing conditions. There may also be metal (either Pt or Pd, but more likely Pt) present in the vapor phase near the catalyst support that could affect catalytic activity. Even if material loss by vaporization is less significant for bulk conditions relevant to catalysis due to redeposition, the *in-situ* experiments suggest that movement of the catalyst due to vaporization and redeposition could play an important role in catalyst structural evolution, a role that was previously ascribed to migration in *ex-situ* experiments. One possible implication is that the catalyst support needs to serve as a nucleation center for redeposition of the catalyst from the vapor phase. In addition, slow dissolution of catalyst by diffusion into the support or decomposition into single atoms may be another structural evolution pathway by which catalyst activity degrades.[43, 44] In a real gasoline engine, cycles of oxidizing and reducing conditions are likely to help prevent material loss from the observed rapid

catalyst volatilization in Figure 2. However, the high operating temperatures and periods of highly oxidative conditions suggest that *in-situ* observation of redox catalysis may have advantages in capturing the detailed mechanisms (such as vaporization) of catalyst structural changes. At present, it is not possible to reproduce cycles of oxidative and reducing conditions at the frequencies (~ 1 Hz) relevant to gasoline engines. However, this may be possible in the future by periodically introducing hydrocarbons as a reductant.

Thus, in these experiments, Ostwald ripening, in which larger particles grow at the expense of smaller particles, does not appear to be the dominant mechanism of structural change. Instead, particles appear to either vaporize or decrease in size. One possible hypothesis is that the small size of Pt/Pd nanoparticles increases their vapor pressure due to the Gibbs-Thomson effect. This effect is compounded by the instability and volatility of PtO_2, which forms more rapidly on smaller diameter Pt particles during oxidation.[45-47] As the catalyst is heated, the smaller nanoparticles would evaporate at lower temperatures, consistent with observations that many small Pt/Pd nanoparticles disappear. Furthermore, the observed decrease in particle aspect ratio, which is a proxy for the surface area to volume ratio, suggests that surface energy could be a driving force for the observed structural change. This, in turn, is consistent with the Gibbs-Thomson effect. The particle aspect ratio is obtained via machine learning image segmentation, which is helpful for developing improved quantitative understanding of catalyst structural evolution.[48] To rationalize the observations, it is important to consider that the structural and morphological changes in the catalyst observed both *in-situ* and *ex-situ* are consistent with vaporization induced by a combination of the Gibbs-Thomson effect and chemical oxidation effects. The melting point of Pt and Pd are 1768 °C and 1555 °C, and their vapor pressures are negligible at 700 °C. Assuming solid-liquid interface energies for Pt and Pd of 0.240 J/m^2 and 0.209 J/m^2,[49] we calculate that the dependence of relative decrease in melting point on particle sizes are about the same for both elements. For 10 nm, 5 nm, 2 nm, and 1 nm diameter nanoparticles, the melting point decreases by 4%, 9%, 20%, and 40%, respectively. This suggests that evaporation of either metal due to the Gibbs-Thomson effect alone is highly unlikely for particles with diameters greater than 1-2 nm. Thus, the main driving force for vaporization of larger particles is likely chemical. Remaining Pt-rich catalyst particles (Figure 8f) post-oxidation suggests that some large particles either avoid oxide formation or vaporize very slowly after oxidizing. The results are consistent with the kinetics of PtO_2 formation and volatilization on Pt nanoparticles exhibiting size dependence. McCabe et al. observe that Pt oxidation is self-limited due to surface passivation, that the oxide layer is a mixture of stoichiometric PtO_2 and chemisorbed oxygen, and that the stability of the oxide correlates inversely with the particle size based on reduction kinetics.[47] The presence of the large remaining Pd-rich catalyst particles could be consistent with Ostwald ripening.

The most important conclusion from the STEM-EDS data of the fresh $Pt/Pd/Al_2O_3$ is that the disappearance of metal catalyst appears to occur independent of either the initial composition or composition distribution, which varies widely in the highly heterogeneous sample. On the other hand, comparison of STEM-EDS data from the oxide support region that does not have easily discernable Pt/Pd catalyst particles before and after oxidation suggests that both Pt and Pd become more sparse/dilute on the oxide support, consistent with vaporization. The presence of Pd after oxidation is consistent with redistribution of the metal via diffusion. On the other hand, previous studies of Pt/SiO_2 at 650°C showed Ostwald ripening to be the primary phenomenon;[50] the differences in the materials system and experiment temperature could account for this. Our observation of the rapid onset of vaporization at ~ 700°C suggests that the small temperature change significantly changes the dominant mechanisms for structural evolution. This is important because automotive emission controls catalysts can experience temperatures higher than 700°C.

The observations show that smaller catalysts reappear during the reduction process; this behavior is expected in similar catalyst materials.[51] This could be consistent with a process whereby metal dissolved in the support through bulk diffusion during oxidation returns to the surface and aggregates. As the engine undergoes lean/rich or oxidative/reductive cycles, some metal catalyst particles may cycle between aggregated particles on the surface and being dispersed or dissolved on the oxide support surface or bulk, respectively. Notably, the development of catalyst systems that intentionally undergo dissolution into an oxide support – so called "intelligent catalysts" [52] – is presently an important topic in automotive catalysis.[53] Our observations reflect expectations of catalyst regeneration under reductive conditions. Combined with the observations of the catalyst under oxidation, we hypothesize that vaporization and redeposition play a role in catalyst structural evolution, and that diffusion of Pt and Pd likely cycle between dispersion and aggregation under oxidative and reductive conditions, respectively. Although the conditions of the *in-situ* experiment favor vaporization, the temperatures attained are still lower than the maximum temperatures of catalytic converters. A corollary is that loss of material through evaporation of the catalyst likely occurs to some degree even if redeposition occurs, and thus the performance of the Pt/Pd catalyst will irreversibly decrease slowly over time.

Conclusions

Using an *in-situ* gas cell in the TEM, the structural changes in a Pt/Pd catalyst supported on Al_2O_3 are observed in real-time, providing the intermediate stages of the morphology between the fresh and aged structure. Metal disappearance through volatilization and diffusion are observed at temperatures as low as 700°C, consistent with increased volatility of the catalyst due to the Gibbs-Thomson effect and chemical effects of oxidation. The complete loss of metal in regions of the sample implies two effects: 1) preferential vaporization of Pt and 2) diffusion of

Pt/Pd through the surface or bulk from catalyst particles to the surrounding oxide support. This data suggests that vaporization and redeposition play a role in catalyst structural evolution. Finally, reductive conditions were observed to regenerate the catalyst by returning the morphology to one similar to that of its fresh condition. It is likely important to cycle rapidly between oxidizing and reducing conditions to accurately capture *operando* conditions. The *in-situ* gas cell is well-suited to characterizing changes in the catalyst as it dynamically alternates between vaporization and redeposition/re-nucleation. However, the cycle frequency (~1 Hz) will require some modification of the gas delivery apparatus. Furthermore, *in-situ* TEM generates data that can be mined using image segmentation. The information includes shape factors such as aspect ratio. While changes in some of these variables are apparent in the micrographs, incorporating the data into a model for catalyst particle evolution has the potential to reveal subtle dependencies of particle morphology on redox conditions. We observed a decrease in surface area to volume ratio of Pt/Pd particles supported on Al_2O_3 consistent with surface energy as a driving force for catalyst structural evolution. This is also consistent with metal vaporization from oxidation and the Gibbs-Thomson effect, both of which affect or are affected by the surface energy of the metal particle. For industrial application of *in-situ* TEM methodology to catalyst aging tests, data from the gas cell can be accumulated to provide large statistical sampling over many experiments. The method is promising for improving understanding of catalyst dynamics through faithful representation of *operando* conditions, which can significantly improve understanding of underlying catalyst degradation mechanisms.

Acknowledgements

The authors acknowledge funding from BASF. This work was carried out in part at the Singh Center for Nanotechnology, which is supported by the NSF National Nanotechnology Coordinated Infrastructure Program under grant NNCI-1542153. Transmission electron microscopy was performed in facilities supported by the NSF MRSEC Program under Award No. DMR-1120901. A.F. acknowledges support by Integrated Mesoscale Architectures for Sustainable Catalysis (IMASC), an Energy Frontier Research Center funded by DOE, Office of Science, BES under Award # DE-SC0012573.

Conflicts of interest

There are no conflicts to declare.

Notes and References

‡ Footnotes relating to the main text should appear here. These might include comments relevant not central to the matter under discussion, limited experimental and spectral data, and crystallographic data.
§
§§

1. K. Ramanathan and S. H. Oh, *Chem. Eng. Res. Des.*, 2014, **92**, 350-361.
2. M. L. Taheri, E. A. Stach, I. Arslan, P. A. Crozier, B. C. Kabius, T. LaGrange, A. M. Minor, S. Takeda, M. Tanase and J. B. Wagner, *Ultramicroscopy*, 2016, **170**, 86-95.
3. G. Graham, H.-W. Jen, O. Ezekoye, R. Kudla, W. Chun, X. Pan and R. McCabe, *Catal. Lett.*, 2007, **116**, 1-8.
4. P. Castellazzi, G. Groppi and P. Forzatti, *Appl. Catal. B*, 2010, **95**, 303-311.
5. A. T. Gremminger, H. W. P. de Carvalho, R. Popescu, J.-D. Grunwaldt and O. Deutschmann, *Catal. Today*, 2015, **258**, 470-480.
6. G. Lapisardi, P. GÚlin, A. Kaddouri, E. Garbowski and S. Da Costa, *Top. Catal.*, 2007, **42**, 461-464.
7. T. R. Johns, R. S. Goeke, V. Ashbacher, P. C. Thüne, J. Niemantsverdriet, B. Kiefer, C. H. Kim, M. P. Balogh and A. K. Datye, *J. Catal.*, 2015, **328**, 151-164.
8. Z. Abbasi, M. Haghighi, E. Fatehifar and S. Saedy, *J. Hazard. Mater.*, 2011, **186**, 1445-1454.
9. M. J. Hazlett, M. Moses-Debusk, J. E. Parks II, L. F. Allard and W. S. Epling, *Appl. Catal. B*, 2017, **202**, 404-417.
10. J. Kim, Y. Kim, M. H. Wiebenga, S. H. Oh and D. H. Kim, *Appl. Catal. B*, 2019, **251**, 283-294.
11. R. S. Monteiro, L. C. Dieguez and M. Schmal, *Catal. Today*, 2001, **65**, 77-89.
12. X. Chen, Y. Cheng, C. Y. Seo, J. W. Schwank and R. W. McCabe, *Appl. Catal. B*, 2015, **163**, 499-509.
13. M. Kaneeda, H. Iizuka, T. Hiratsuka, N. Shinotsuka and M. Arai, *Appl. Catal. B*, 2009, **90**, 564-569.
14. C. Carrillo, A. DeLaRiva, H. Xiong, E. J. Peterson, M. N. Spilde, D. Kunwar, R. S. Goeke, M. Wiebenga, S. H. Oh and G. Qi, *Appl. Catal. B*, 2017, **218**, 581-590.
15. C. Carrillo, T. R. Johns, H. Xiong, A. DeLaRiva, S. R. Challa, R. S. Goeke, K. Artyushkova, W. Li, C. H. Kim and A. K. Datye, *J. Phys. Chem. Lett.*, 2014, **5**, 2089-2093.
16. M. R. Ward, T. Hyde, E. D. Boyes and P. L. Gai, *ChemCatChem*, 2012, **4**, 1622-1631.
17. M. Lyubovsky, L. Pfefferle, A. Datye, J. Bravo and T. Nelson, *J. Catal.*, 1999, **187**, 275-284.
18. N. Castillo, J. Tenorio-Lopez, M. Martínez Ortiz, L. García, R. Pérez and A. Conde, *Acta Microsc.*, 2009, **18**.
19. L. C. Gontard, L. Y. Chang, C. J. Hetherington, A. I. Kirkland, D. Ozkaya and R. E. Dunin-Borkowski, *Angew. Chem. Int. Ed.*, 2007, **46**, 3683-3685.
20. S. B. Simonsen, I. Chorkendorff, S. Dahl, M. Skoglundh, J. Sehested and S. Helveg, *J. Am. Chem. Soc.*, 2010, **132**, 7968-7975.
21. C. Dessal, A. Sangnier, C. Chizallet, C. Dujardin, F. Morfin, J.-L. Rousset, M. Aouine, M. Bugnet, P. Afanasiev and L. Piccolo, *Nanoscale*, 2019, **11**, 6897-6904.
22. K. K. Bando, T. Kawai, K. Asakura, T. Matsui, L. Le Bihan, H. Yasuda, Y. Yoshimura and S. T. Oyama, *Catal. Today*, 2006, **111**, 199-204.
23. U. Jung, A. Elsen, Y. Li, J. G. Smith, M. W. Small, E. A. Stach, A. I. Frenkel and R. G. Nuzzo, *ACS Catal.*, 2015, **5**, 1539-1551.
24. F. Bernardi, M. Alves and J. Morais, 2009.
25. V. Petkov and S. Shastri, *Phys. Rev. B*, 2010, **81**, 165428.
26. N. M. Martin, J. Nilsson, M. Skoglundh, E. C. Adams, X. Wang, G. Smedler, A. Raj, D. Thompsett, G. Agostini and S. Carlson, *Catal. Struct. React.*, 2017, **3**, 24-32.

27. Y. Liang, C. Ou, H. Zhang, X. Ding, M. Zhao, J. Wang and Y. Chen, *Ind. Eng. Chem. Res.*, 2018, **57**, 3887-3897.
28. M. Haneda, M. Sasaki and H. Hamada, *J. Japan Pet. Inst.*, 2015, **58**, 205-217.
29. R. Navarro, B. Pawelec, J. Trejo, R. Mariscal and J. Fierro, *J. Catal.*, 2000, **189**, 184-194.
30. F. Behafarid, S. Pandey, R. E. Diaz, E. A. Stach and B. R. Cuenya, *Phys. Chem. Chem. Phys.*, 2014, **16**, 18176-18184.
31. *USA Pat.,* 8329607, 2012.
32. *USA Pat.,* 10260395, 2019.
33. A.-C. Yang, T. Choksi, V. Streibel, H. Aljama, C. J. Wrasman, L. T. Roling, E. D. Goodman, D. Thomas, S. R. Bare, R. S. Sánchez-Carrera, A. Schäfer, Y. Li, F. Abild-Pedersen and M. Cargnello, *Proc. Natl. Acad. Sci. U.S.A.*, 2020, **117**, 14721-14729.
34. I. Arganda-Carreras, V. Kaynig, C. Rueden, K. W. Eliceiri, J. Schindelin, A. Cardona and H. Sebastian Seung, *Bioinformatics*, 2017, **33**, 2424-2426.
35. S. D. House, C. S. Bonifacio, R. V. Grieshaber, L. Li, Z. Zhang, J. Ciston, E. A. Stach and J. C. Yang, *Ultramicroscopy*, 2016, **169**, 22-29.
36. H. L. Xin, K. Niu, D. H. Alsem and H. Zheng, *Microsc. Microanal*, 2013, **19**, 1558-1568.
37. M. Kolwas, D. Jakubczyk, T. Do Duc and J. Archer, *Soft Matter*, 2019, **15**, 1825-1832.
38. G. Cliff and G. W. Lorimer, *J. Microsc.*, 1975, **103**, 203-207.
39. E. D. Goodman, A. A. Ye, A. Aitbekova, O. Mueller, A. R. Riscoe, T. N. Taylor, A. S. Hoffman, A. Boubnov, K. C. Bustillo, M. Nachtegaal, S. R. Bare and M. Cargnello, *J. Chem. Phys.*, 2019, **151**, 154703.
40. T. R. Johns, J. R. Gaudet, E. J. Peterson, J. T. Miller, E. A. Stach, C. H. Kim, M. P. Balogh and A. K. Datye, *ChemCatChem*, 2013, **5**, 2636-2645.
41. D. Kunwar, C. Carrillo, H. Xiong, E. Peterson, A. DeLaRiva, A. Ghosh, G. Qi, M. Yang, M. Wiebenga, S. Oh, W. Li and A. K. Datye, *Appl. Catal. B*, 2020, **266**, 118598.
42. A. Ghosh, H. Pham, J. Higgins, F. Van Swol, A. DeLaRiva, M. Melton, D. Kunwar, G. Qi, S. H. Oh, M. Wiebenga, W. Li and A. K. Datye, *Appl. Catal. A*, 2020, **607**, 117858.
43. C. K. Narula, L. F. Allard, M. Moses-DeBusk, G. M. Stocks and Z. Wu, *Sci. Rep.*, 2017, **7**, 560.
44. E. D. Goodman, A. C. Johnston-Peck, E. M. Dietze, C. J. Wrasman, A. S. Hoffman, F. Abild-Pedersen, S. R. Bare, P. N. Plessow and M. Cargnello, *Nat. Catal.*, 2019, **2**, 748-755.
45. R. Banerjee, D. A. Chen, S. Karakalos, M.-L. C. Piedboeuf, N. Job and J. R. Regalbuto, *ACS Appl. Nano Mater.*, 2018, **1**, 5876-5884.
46. R. Banerjee, Q. Liu, J. M. M. Tengco and J. R. Regalbuto, *Catal. Lett.*, 2017, **147**, 1754-1764.
47. R. W. McCabe, C. Wong and H. S. Woo, *J. Catal.*, 1988, **114**, 354-367.
48. J. P. Horwath, D. N. Zakharov, R. Mégret and E. A. Stach, *NPJ Comput. Mater.*, 2020, **6**, 1-9.
49. T. Tanaka, J. Lee and P. R. Scheller, in *Treatise on Process Metallurgy*, ed. S. Seetharaman, Elsevier, Boston, 2014, DOI: https://doi.org/10.1016/B978-0-08-096984-8.00025-2, pp. 61-77.
50. S. B. Simonsen, I. Chorkendorff, S. Dahl, M. Skoglundh, J. Sehested and S. Helveg, *J. Catal.*, 2011, **281**, 147-155.
51. E. J. Peterson, A. T. DeLaRiva, S. Lin, R. S. Johnson, H. Guo, J. T. Miller, J. Hun Kwak, C. H. F. Peden, B. Kiefer, L. F. Allard, F. H. Ribeiro and A. K. Datye, *Nat. Commun.*, 2014, **5**, 4885.
52. M. Uenishi, H. Tanaka, I. Tan, M. Taniguchi, N. Kajita, M. Kimura, K. Narita and H. Suzuki, *AutoTechnology*, 2007, **7**, 44-47.
53. Y. Nishihata, J. Mizuki, T. Akao, H. Tanaka, M. Uenishi, M. Kimura, T. Okamoto and N. Hamada, *Nature*, 2002, **418**, 164-167.